Can natural H_2 be considered renewable ? The reference case of a deep aquifer in an intracratonic sedimentary basin

Fabrice Brunet[1], Benjamin Malvoisin[1]
[1] Univ. Grenoble Alpes, USMB, CNRS, IRD, UGE, ISTerre, Grenoble, France
Correspondence to: Fabrice Brunet, fabrice.brunet@univ-grenoble-alpes.fr

Supplementary Material

Contents

1 Calculation of radiolytic H_2 flux

The rate of H_2 formation by radiolysis in the fluid ($Y_{H_2,f}$ in mol.m^{-3}.s^{-1}) is the dose rate absorbed by water (D_{ri} for radionuclide r and radiation type i in J.m^{-3}.s^{-1}) multiplied by the G-value, the number of moles of H_2 created per joule of radiation type i ($G_{H_2,i}$). Radiolytic products are generated for each radionuclide decay (^{40}K, ^{232}Th, ^{235}U and ^{238}U are considered here) and each type of ionizing radiation particle, leading to the following total product rate for H_2:

$$Y_{H_2,f} = \sum_i \left(G_{H_2,i} \sum_r D_{r,i} \right) \tag{S1}$$

This yield of H_2 formation in the fluid by radiolysis can be converted in a yield in the porous material ($Y_{H_2,s}$) by using:

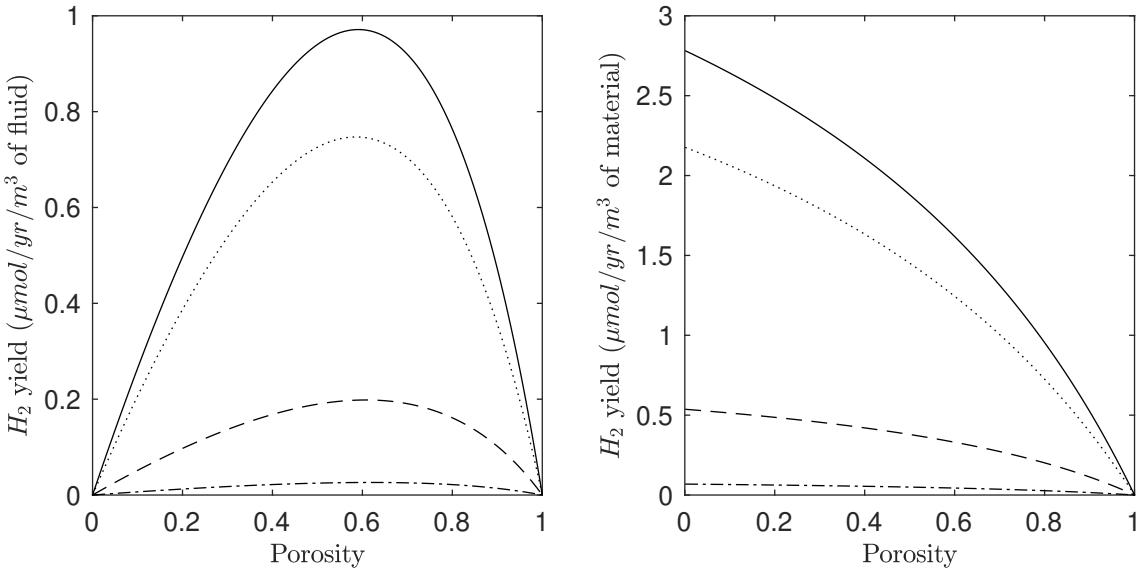

Figure S1: H_2 yield of radiolysis in the upper crust expressed for the pore fluid (a) and the whole porous material (b). The yield for all radiations (plain line), α radiation (dotted line), β radiation (dashed line) and γ radiation (dash-dotted line) are displayed.

$$Y_{H_2,s} = \frac{Y_{H_2,f}}{\phi} \tag{S2}$$

where ϕ is the porosity.

Bouquet et al. [2017] explicitly take into account the effect of porosity:

$$D_{r,i} = \frac{\rho_s X_r \lambda_r E_{r,i}}{\frac{1}{1-\phi} + \frac{\rho_s}{S_i \rho_w \phi}} \tag{S3}$$

where ρ_s and ρ_w are the solid and the water density (kg.m^{-3}), respectively, X_r is the concentration in radionucleide r in the solid (mol.kg^{-1}), λ_r is the decay constant (s^{-1}), $E_{r,i}$ is the energy decay associated with radionuclide r emitting radiation type i (J.mol^{-1}) and S_i is the stopping power of the solid. The values of all the parameters used here are provided in Tables S1 and S2. The element concentrations of the upper crust were selected, which are higher than those of the lower crust. The estimated yields of H_2 production by radiolysis are thus maxima.

Figure S1 provides the dependency of H_2 production rate on porosity. The main radiation participating in H_2 production during water radiolysis are α particles. When considering the fluid only, H_2 yield strongly depends on porosity and displays a bell

Radionucleide	Conc. upper crust (ppm)[a]	Nat. abund. (%)[b]	X_rx10^5 (mole.kg^{-1})	$E_{r,\alpha}$x10^{-12} (J.mol^{-1})[c]	$E_{r,\beta}$x10^{-12} (J.mol^{-1})[c]	$E_{r,\gamma}$x10^{-12} (J.mol^{-1})[c]	λx10^{17} (s^{-1})[c]
^{40}K	28650	0.0117	8.3877	0	0.1135	0.0151	1.7584
^{232}Th	10.3	100	4.4389	3.4686	0.2741	0.2166	0.157
^{235}U	2.5	0.72	0.0077	3.2833	1.008	0.0531	3.1221
^{238}U	2.5	99.27	1.0426	4.1459	0.5879	0.1643	0.4928

[a]Wedepohl [1995]; [b]Lide [1995]; [c]Bouquet et al. [2017]

Table S1: Radionucleide properties.

Radiation	S_i[a]	$G_{H_2,i}$x10^8 (mol.J^{-1})[b]
α	1.5	9.9499
β	1.25	6.2187
γ	1.14	4.1458

[a]Hofmann, 1992; [b]Lin et al. [2005]

Table S2: Radiation-related properties.

shaped curve with porosity similar to the one calculated by Bouquet et al. [2017]. When considering the whole porous material, H_2 yield only slightly decreases with porosity for $\phi < 0.5$. For example, the total H_2 yields of the porous rock are of 2.78 and 2.77 µmol.m^{-3}yr^{-1} for porosities of 0.1 % and 1 %, respectively.

To determine the evolution with depth of the H_2 concentration ([H_2] in mol.m^{-3}), we used a one-dimensional model of H_2 diffusion in a connected network of pores:

$$\frac{\partial\left(\phi\left[H_2\right]\right)}{\partial t}+\frac{\partial J}{\partial z}=S \tag{S4}$$

where S is a sink/source term, z is the depth (m) and J is the flux of H_2 (J_{H2} in mol.m^{-2}.s^{-1}) given by Fick's law:

$$J_{H_2}=-\phi D_{H_2}\frac{\partial\left[H_2\right]}{\partial x} \tag{S5}$$

with D_{H_2} the diffusion coefficient of H_2 in the fluid (m^2.s^{-1}). The expression of D_{H_2} provided in Kallikragas et al. [2014] was used to compute D_{H_2} at 298.15 K. S includes H_2 production by radiolysis modelled with equations (S1) and (S3). We also considered H_2 consumption by chemical reactions between the products of radiolysis. Most of the products of radiolysis are highly unstable in water and react together at short timescale.

One hour after radiolysis, H_2, O_2 and H_2O_2 are the main remaining reaction products (Pastina and LaVerne [2001]). These three latter reaction products can further react together to form H_2O according to the two following reactions:

$$H_{2,aq} + \frac{1}{2}O_{2,aq} = H_2O \tag{S6}$$

$$H_2O_{2,aq} = H_2O + \frac{1}{2}O_{2,aq} \tag{S7}$$

Foustoukos et al. [2011] measured the kinetics of Reactions (S6) and (S7) and found that Reaction (S7) proceeds approximately one order of magnitude faster than Reaction (S6). Reaction (S6) thus controls the overall rate of water formation by the product of radiolysis at geological timescale. Foustoukos et al. [2011] provided a first-order reaction rate for this latter reaction:

$$\frac{\partial\,[H_2]}{\partial t} = -A\exp\left(-\frac{E_a}{RT}\right)[H_2] \tag{S8}$$

where A is a pre-exponential factor (0.15 s^{-1}), E_a is the activation energy (24 $kJ.mol^{-1}$), R is the gas constant and T is the temperature (K). The dependency of T with depth was expressed as:

$$T = T_0 + \theta z \tag{S9}$$

where T_0 is the temperature at the surface (298 K) and θ is the geothermal gradient (in $K.m^{-1}$).

Considering steady-state conditions and using equations (S4), (S5), (S8) and (S9) allow to obtain a differential equation for H_2 concentration by excluding H_2 consumption:

$$D_{H_2}\frac{\partial^2\,[H_2]}{\partial z^2} + Y_{H_2,f} = 0 \tag{S10}$$

or by considering, in addition, H_2 consumption during reaction with O_2 formed by radiolysis:

$$D_{H_2}\frac{\partial^2 [H_2]}{\partial z^2} + Y_{H_2,f} - A\exp\left(-\frac{E_a}{R\left(T_0+\theta z\right)}\right)[H_2] = 0 \tag{S11}$$

Equations (S10) and (S11) were solved numerically with a solver for boundary value problems using a fourth-order method in Matlab®. We used as boundary conditions zero H_2 concentration at the surface ($[H_2]_{(z=0)}$=0) and no H_2 flux at 20 km depth ($\frac{\partial[H_2]}{\partial z}|_{z=20\text{ km}} = 0$). The geothermal gradient is fixed to 30 °C.km^{-1}. Figure 2 provides calculations of concentration profiles when considering or not H_2 consumption through chemical reaction with O_2 (solutions to equations (S10) and (S11)). When excluding consumption by reaction with O_2, the calculated H_2 concentration is of the order of 1 mol.kg^{-1} and increases with depth up to a value of 2.8 mol.kg^{-1} at 20 km depth (Figure 2a). These latter values are ca. 11 orders of magnitude higher than when considering consumption through reaction with O_2 (Figure 2b). The concentration decreases with depth, due to the thermal activation of Reaction (S6) whereas radiolysis rate does not depend on temperature. The concentration profile is well modelled by H_2 concentration at the equilibrium between production by radiolysis and consumption through reaction with O_2:

$$[H_2]_{eq} = \frac{Y_{H_2,f}}{A\exp\left(-\frac{E_a}{R(T_0+\theta z)}\right)} \tag{S12}$$

2 Thermochemical modeling of low-temperature serpentinization

Calculations are performed with Perple_X version 7.1.4 Connolly [2005]. The fluid is modelled with a generic hydrid fluid equation of state solution model for a pure water solvent (WADDAH in Perple_X). The database was derived from Holland and Powell [2011] for solid phases and the Deep Earth Water model of Huang and Sverjensky [2019] for aqueous species including H_2 (DEW19HP622ver_elements.dat in Perple_X). A new $Fe(OH)_2$ endmember was introduced in the database. The

C_p function of $Fe(OH)_2$ is calculated, following McCollom and Bach [2009], as: $C_{p,Fe(OH)_2} = C_{p,Mg(OH)_2} + 1/3\left(C_{p,greenalite} - C_{p,lizardite}\right)$. The α_0, κ_0, κ_0' and κ_0'' parameters in the equation of state of $Fe(OH)_2$ [Holland and Powell, 2011] are set as equal to those of brucite ($Mg(OH)_2$). We used the standard state enthalpy and third law entropy for $Fe(OH)_2$ fitted with the experimental dataset of Carlin et al. [2024]. The procedure for fitting the parameters is the same of the one described in Carlin et al. [2024] but with the thermodynamic data for magnetite, H_2O and H_2 from the DEW19HP622ver_elements database. Awaruite, $Ni(OH)_2$ and nepouite were added in the database with the thermodynamic data provided in Evans et al. [2017] and Palmer and Gamsjäger [2010]. Nepouite thermodynamic properties were calculated as linear combinations of brucite, forsterite and Ni_2SiO_4 thermodynamic properties.

We used solid solution models for olivine [Holland and Powell, 1998], brucite (ideal with brucite, amakinite and $Ni(OH)_2$ as endmembers), orthopyroxene [Holland and Powell, 1996], talc (ideal), and lizardite modified from Evans et al. [2013] by adding nepouite endmember. The lizardite solid solution model of Evans et al. [2013] considers ferri-tschermak substitution. Olivine and orthopyroxene have an Mg/(Mg+Fe) ratio of 0.91 and olivine has a Ni/(Ni + Fe + Mg) ratio of 0.004. A water-to-rock mass ratio of 0.2 was used corresponding to the minimum water to rock ratio for complete olivine hydration. Calculation was performed along a temperature gradient of 30 °C/km with a surface temperature of 20 °C in the subcritical domain of the H_2 - H_2O binary. Equilibrium mineral modes for harzburgite and for a water-to-rock of 0.2 are displayed along the geotherm on Figure S2. Perple_X outputs indicate that [H_2] is the highest at low water-to-rock ratio as already shown by Klein et al. [2009]. At the minimum water-to-rock mass (wr) ratio used here (i.e., 0.2), harzburgite serpentinisation produces awaruite (Ni_3Fe). Considering the relatively small absolute amount of H_2 produced in the Ni-free system, i.e., < 300 mmole H_2/l (or < 60 mmole H_2 /kg of rock) at 7000 m for a wr ratio of 0.2, the formation of awaruite from the Ni initially present in olivine can drag H_2 to even lower concentrations even though it

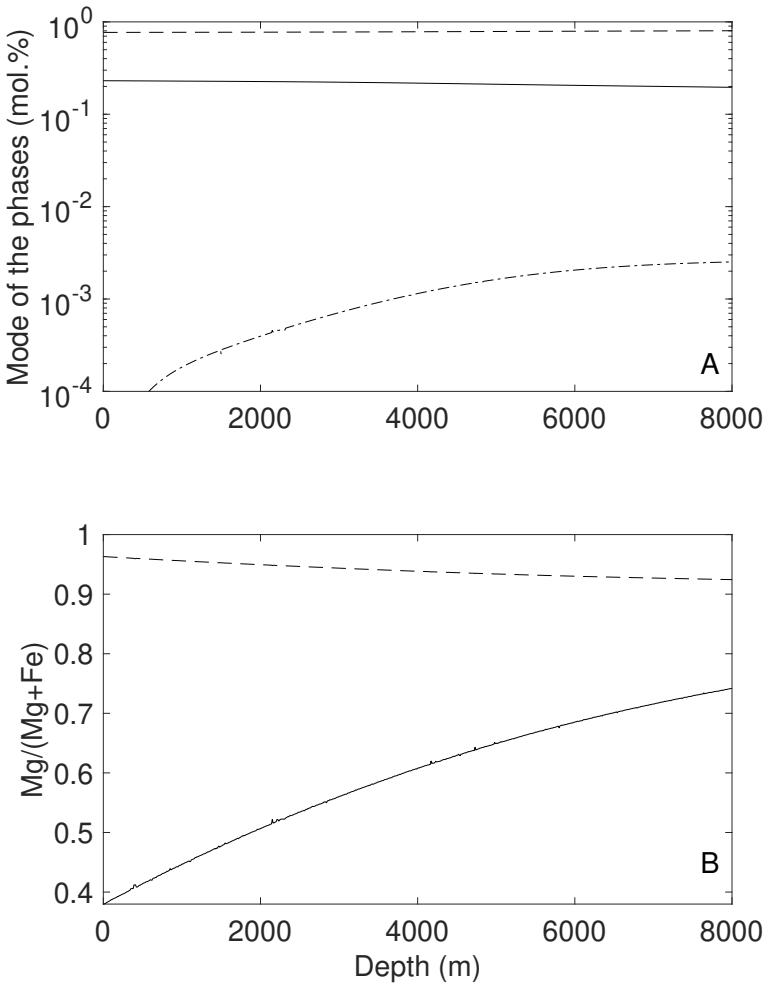

Figure S2: Predicted system composition as a function of depth for the serpentinization of a simplified harzburgite. A: phase modes (mol.%). The plain, dashed and dotted-dashed lines corresponds to the modes of brucite, serpentine and awaruite, respectively. B: mineral composition (Mg/(Mg+Fe) molar ratio). The plain and dashed lines correspond to brucite and serpentine compositions, respectively. Water-to-rock mass ratio is 0.2.

represents less than 1 mol.% of the serpentinised rock. The dependency of equilibrium [H_2] with initial NiO content in olivine is depicted on Figure S3.

3 Aquifer parameterization and H_2 flux calculation

The simplified aquifer has been parameterized by considering a production at a depth > 3,000 m in order for saturation to be potentially achieved with the considered H_2-production processes. The temperature evolution along the aquifer is calculated assuming a geothermal gradient of 30 °C/km with a surface temperature of 20 °C. In that case, H_2 Production Zone, or PZ, is at a too high temperature for H_2 microbial

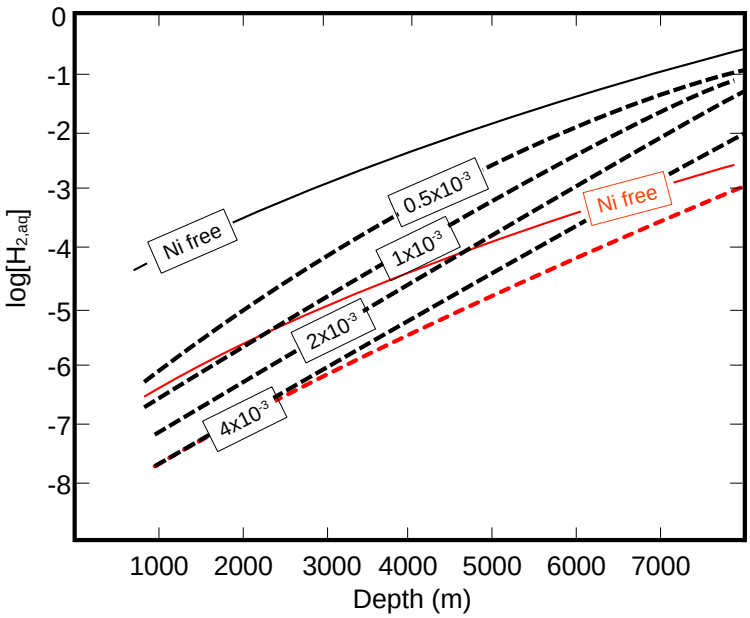

Figure S3: Natural logarithm of $[H_2]$ as a function of Production Zone depth. Dashed lines correspond to X_{Ni} in harzburgite olivine, X_{Ni} = Ni/(Mg+Fe+Ni) of 0.0005, 0.001, 0.002 and 0.004 (wr ratio = 0.2). The thin lines correspond to a Ni-free harzburgite for two wr ratios (0.2, black; 1.0, red). The $[H_2]$ = f(depth) used in the aquifer model corresponds to X_{Ni} = 0.004 and wr ratio = 0.2.

consumption to be effective. For simplification the production zone is supposed to be isothermal. The aquifer has a constant dip angle (α) and flows along the x axis with x_0 as origin at the outflow of the PZ. Microbial activity (H_2 consumption) starts at $x \geq x_{bio}$, i.e., for $T \leq 100$ °C. For $0 \leq x < x_{bio}$ (Abiotic Zone),

H_2 accumulation requires H_2 saturation at some levels (x_{sat}) with $x_{sat} = x_0$ if saturation occurs in the PZ, $0 < x_{sat} < x_{bio}$ if it is achieved in the Abiotic Zone or $x_{sat} > x_{bio}$ if H_2 saturation occurs in a temperature range that is compatible with microbial activity. Any dissolved H_2 that is transported beyond $x = x_{sat,max}$ is lost to the system (Figure S4).

If H_2 saturation is achieved for $x \geq x_{bio}$, $[H_2](x)$ follows the H_2 solubility relationship in the form $[H_{2,\mathrm{sat}}] = Ax + B$, fitted to the model of Lopez-Lazaro et al. (2019). At the same time, aqueous H_2 consumption by microorganisms proceeds as long as H_2 gas is present at x. As soon as H_2 gas is entirely consumed,

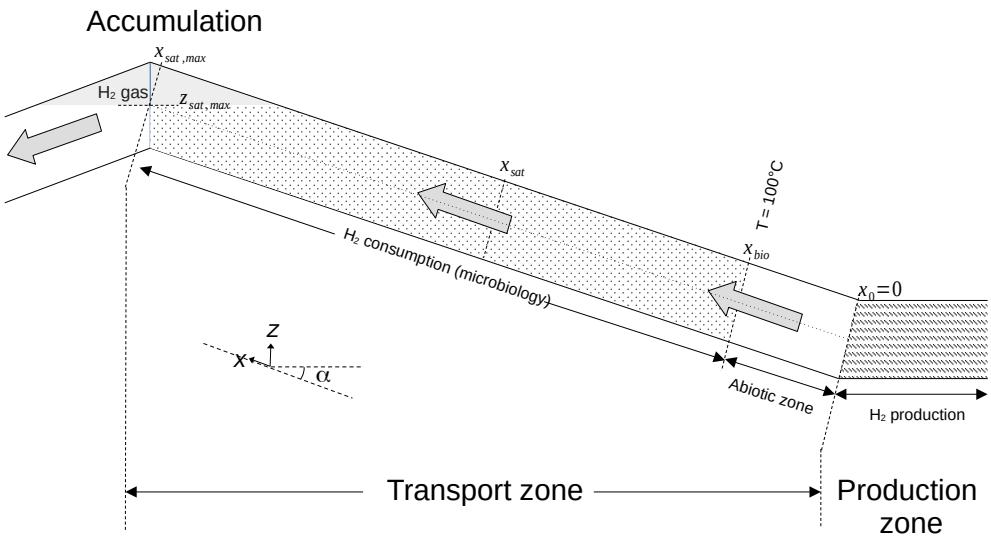

Figure S4: Geometrical parameterization of the 1-D aquifer with Production Zone, Transport Zone and gas accumulation.

$[H_2](x)$ leaves the saturation line and becomes solely controlled by H_2 consumption. The presence or absence of excess gas is verified at each numerical iteration by mass balance.

The bio-consumed H_2 flux (H_2BC_{flux}) is calculated by numerical integration of the expressed below:

$$H_2BC_{flux}(x) = -U \int_0^x (\frac{\partial [H_2](x)}{\partial t} dx \tag{S13}$$

with $\frac{\partial [H_2](x)}{\partial t}$ calculated from S12 and $[H_2](x) = [H_2]_{sat}$. Otherwise, if H_2 saturation is not achieved for $x_{sat} \geq x_{bio}$,with $[H_2](x)$ calculated from the integrated form of S12.

$$H_2BC_{flux}(x) = U([H_2](x) - [H_2](x = x_{bio})) \tag{S14}$$

with $[H_2](x)$ calculated from the integrated form of S12.

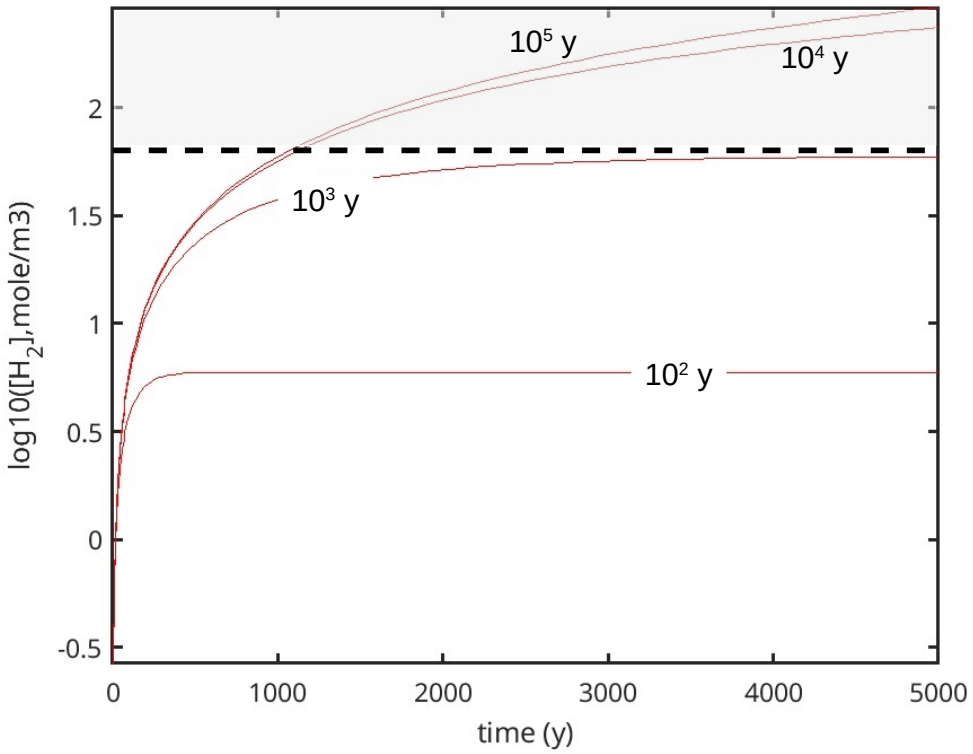

Figure S5: Transient H_2 concentration in the Production Zone. $[H_2]$ time evolution for a PZ located at 7,000 m. Aquifer renewal times are varied from 10^2 to 10^5 year. $[H_{2,aq}]_{max}$ which is the maximum H_2 concentration that can be reached upon olivine serpentinization, is noted with a horizontal dashed line (i.e., $[H_2]$ in grey area are not attained). This maximum concentration is achieved after ca. 1000 years for renewal time of above 10^3 years only. Then, if thermochemical equilibrium is achieved, H_2 concentration is expected to remain constant and a steady-state is reached.

For $x > x_{sat,max}$, the remaining $H_{2,aq}$ dissolved in water escapes the H_2 catchment zone with a flux equals to U. $[H_2](x = x_{sat,max})$ (Figure S4).

4 PZ geometry and fractures network

Since the PZ is located in fractured rocks, the notion of PZ volume needs to be clarified. Without a description of the fracture network and hydraulic properties, all fractures are assumed to have the same porosity ϕ_{FPZ}. The intersection between the fractures of the PZ surface and the surface perpendicular to the aquifer flow is S_{FPZ}. Based on the assumption of continuous water flow-rate and H_2 flux between

fractured PZ and aquifer Transport Zone (Figure S3), the aquifer porosity (ϕ_{aq}) and cross-section area (S_{aq}), and the PZ fractures porosity (ϕ_{FPZ}) and cross-section area (S_{FPZ}) are related:

$$S_{\text{aq}}.\phi_{\text{aq}} = S_{\text{FPZ}}.\phi_{\text{FPZ}} \tag{S15}$$

S_{FPZ} is the fraction (K) of the total PZ area (S_{PZ}) hosting the fractures network that is hydraulically connected to the aquifer. With $0 < K \leq 1$:

$$S_{\text{FPZ}} = K.S_{\text{PZ}} \tag{S16}$$

Then the relevant PZ volume (V_{PZ}) can be calculated as

$$V_{\text{PZ}} = \frac{PZ_{length}.S_{aq}}{K}.\frac{\phi_{\text{aq}}}{\phi_{\text{FPZ}}} \tag{S17}$$

5 PZ lifetime and transitory H_2 production kinetics

The minimum H_2 lifetime, $life_{\text{min}}(T)$, of the Production Zone which is a function of T, can be calculated considering the most H_2 productive olivine reaction, i.e., Equation (4) with 1 mole H_2 produced per 11 moles of olivine (Mg# = 0.9) as

$$life_{\text{min}}(T) = \frac{[Ol]_{rock}}{11.ks^0.exp(\frac{-E_a}{RT}).SA^0{}_{Ol/rock}} \tag{S18}$$

where $SA^0{}_{Ol/rock}$ is the initial surface area of olivine by cubic meter of rock taken as time independent and $[Ol]_{rock}$ is the number of olivine mole per cubic meter of rock. It should be noted that the lifetime calculated in this way may be significantly shorter than the lifetime calculated from steady-state conditions used to derive H_2 fluxes in the model (Figure S5 and 5b).

References

Bouquet, A., Glein, C. R., Wyrick, D. and Waite, J. H. (2017). Alternative Energy: Production of H2 by Radiolysis of Water in the Rocky Cores of Icy Bodies. *The*

Astrophysical Journal Letters 840: L8, doi:10.3847/2041-8213/aa6d56, publisher: The American Astronomical Society.

Carlin, W., Malvoisin, B., Brunet, F., Lanson, B., Findling, N., Lanson, M., Fargetton, T., Jeannin, L. and Lhote, O. (2024). Kinetics of low-temperature h2 production in ultramafic rocks by ferroan brucite oxidation. *Geochemical Perspectives Letters* 29: 27–32, doi:10.7185/geochemlet.2408.

Connolly, J. A. D. (2005). Computation of phase equilibria by linear programming: A tool for geodynamic modeling and its application to subduction zone decarbonation. *Earth and Planetary Science Letters* 236: 524–541, doi:10.1016/j.epsl.2005.04.033.

Evans, K., Powell, R. and Frost, B. (2013). Using equilibrium thermodynamics in the study of metasomatic alteration, illustrated by an application to serpentinites. *Lithos* 168-169: 67–84, doi:10.1016/j.lithos.2013.01.016.

Evans, K. A., Reddy, S. M., Tomkins, A. G., Crossley, R. J. and Frost, B. R. (2017). Effects of geodynamic setting on the redox state of fluids released by subducted mantle lithosphere. *Lithos* 278-281: 26–42, doi:10.1016/J.LITHOS.2016.12.023.

Foustoukos, D. I., Houghton, J. L., Seyfried, W. E., Sievert, S. M. and Cody, G. D. (2011). Kinetics of H2–O2–H2O redox equilibria and formation of metastable H2O2 under low temperature hydrothermal conditions. *Geochimica et Cosmochimica Acta* 75: 1594–1607, doi:10.1016/j.gca.2010.12.020.

Hofmann, B. (1992). Isolated reduction phenomena in red beds: A result of porewater radiolysis? In *International symposium on water-rock interaction*, 503–506.

Holland, T. and Powell, R. (1996). Thermodynamics of order-disorder in minerals: Ii. symmetric formalism applied to solid solutions. *American Mineralogist* 81: 1425–1437.

Holland, T. and Powell, R. (2011). An improved and extended internally consistent thermodynamic dataset for phases of petrological interest, involving a new equation of state for solids. *Journal of metamorphic Geology* 29: 333–383.

Holland, T. J. B. and Powell, R. (1998). An internally consistent thermodynamic data set for phases of petrological interest. *Journal of Metamorphic Geology* 16: 309–343, doi:10.1111/j.1525-1314.1998.00140.x.

Huang, F. and Sverjensky, D. A. (2019). Extended deep earth water model for predicting major element mantle metasomatism. *Geochimica et Cosmochimica Acta* 254: 192–230, doi:10.1016/J.GCA.2019.03.027.

Kallikragas, D. T., Plugatyr, A. Y. and Svishchev, I. M. (2014). High Temperature Diffusion Coefficients for O2, H2, and OH in Water, and for Pure Water. *Journal of Chemical & Engineering Data* 59: 1964–1969, doi:10.1021/je500096r, publisher: American Chemical Society.

Klein, F., Bach, W., Jöns, N., McCollom, T., Moskowitz, B. and Berquó, T. (2009). Iron partitioning and hydrogen generation during serpentinization of abyssal peridotites from 15°n on the mid-atlantic ridge. *Geochimica et Cosmochimica Acta* 73: 6868–6893, doi:10.1016/j.gca.2009.08.021.

Lide, D. R. (1995). *CRC handbook of chemistry and physics: a ready-reference book of chemical and physical data*. CRC press.

Lin, L.-H., Slater, G. F., Sherwood Lollar, B., Lacrampe-Couloume, G. and Onstott, T. C. (2005). The yield and isotopic composition of radiolytic H2, a potential energy source for the deep subsurface biosphere. *Geochimica et Cosmochimica Acta* 69: 893–903, doi:10.1016/j.gca.2004.07.032, number: 4.

McCollom, T. M. and Bach, W. (2009). Thermodynamic constraints on hydrogen generation during serpentinization of ultramafic rocks. *Geochimica et Cosmochimica Acta* 73: 856–875, doi:10.1016/j.gca.2008.10.032.

Palmer, D. A. and Gamsjäger, H. (2010). Solubility measurements of crystalline β-ni (oh) 2 in aqueous solution as a function of temperature and ph. *Journal of coordination chemistry* 63: 2888–2908.

Pastina, B. and LaVerne, J. A. (2001). Effect of Molecular Hydrogen on Hydrogen Peroxide in Water Radiolysis. *The Journal of Physical Chemistry A* 105: 9316–9322, doi:10.1021/jp012245j, publisher: American Chemical Society.

Wedepohl, K. H. (1995). The composition of the continental crust. *Geochimica et cosmochimica Acta* 59: 1217–1232.